





## Control of spin polarization through recollisions

Stefanos Carlström <sup>1,2,\*</sup>, Jan Marcus Dahlström <sup>2</sup>, Misha Yu Ivanov <sup>1,3,4</sup>, Olga Smirnova <sup>1,5</sup> and Serguei Patchkovskii<sup>1</sup>

<sup>1</sup>Max-Born-Institut, Max-Born-Straße 2A, 12489 Berlin, Germany

<sup>2</sup>Department of Physics, Lund University, Box 118, SE-221 00 Lund, Sweden

<sup>3</sup>Department of Physics, Imperial College London, South Kensington Campus, SW72AZ London, United Kingdom

<sup>4</sup>Institut für Physik, Humboldt-Universität zu Berlin, Newtonstraße 15, 12487 Berlin, Germany

<sup>5</sup>Technische Universität Berlin, Ernst-Ruska-Gebäude, Hardenbergstraße 36A, 10623 Berlin, Germany



(Received 26 June 2023; accepted 14 September 2023; published 6 October 2023)

Using only linearly polarized light, we study the possibility of generating spin-polarized photoelectrons from xenon atoms. No net spin polarization is possible, since the xenon ground state is spinless, but when the photoelectrons are measured in coincidence with the residual ion, spin polarization emerges. Furthermore, we show that ultrafast dynamics of the recolliding photoelectrons contribute to an apparent flipping of the spin of the photoelectron, a process that has been completely neglected so far in all analyses of recollision-based processes. We link this phenomenon to the “spin-orbit clock” of the remaining ion. These effects arise already in dipole approximation.

DOI: [10.1103/PhysRevA.108.043104](https://doi.org/10.1103/PhysRevA.108.043104)

### I. INTRODUCTION

Generation of spin-polarized photoelectrons using intense circularly polarized light has recently become a topic of great interest [1–5]. Since the rare gases commonly employed in strong-field ionization experiments are spinless in the ground state, linearly polarized light cannot generate net spin polarization. In this article we show that when the photoelectron is measured in coincidence with the final ion state, the spin polarization approaches 100% in the individual ionization channels (resolved on  $J$  and  $M_J$ ). Furthermore, we link the resulting spin polarization to the rescattering electron imaging the ultrafast hole motion, providing an intuitive picture of electron trajectories that contribute to an apparent spin flip of the detected electron—a signature of recollision-driven coupling between continua with different spins. We find that the spin-flip recollisions are very significant, and that we may exercise precise control over the outcome. This effect, which has so far been overlooked, is important in all recollision-based imaging techniques such as laser-induced electron diffraction [6], electron holography [7], and orbital tomography [8,9].

This article is arranged as follows: Sec. II introduces the computational tools we employ in the calculations, presented in Sec. III. Section IV concludes the article.

### II. THEORY

Our method consistently treats multielectron spin dynamics in strong laser fields, and is thus suitable for our chosen target, xenon. It is based upon the time-dependent configuration-interaction singles (TD-CIS) [10–12]. The equations of motion (EOMs) describe the time evolution of the amplitude  $c_0$  for the Hartree-Fock (HF) reference state, and the particle orbital  $|\tilde{k}\rangle$  emanating from the initially occupied (time-independent) orbital  $|k\rangle$ . Below, we employ Hartree atomic units. Quantities appearing on one side only are summed or integrated over. The different particle-hole channels can couple via both the laser interaction and the Coulomb interaction:

$$\begin{aligned} i\partial_t c_0 &= \langle k | \hat{V}_L | \tilde{k} \rangle, \\ i\partial_t |\tilde{k}\rangle &= (-\epsilon_k + \hat{f})|\tilde{k}\rangle + c_0 \hat{V}_L |k\rangle - \langle l | \hat{V}_L | k \rangle |\tilde{l}\rangle \\ &\quad - (\hat{J}_{lk} - \hat{K}_{lk})|\tilde{l}\rangle - \lambda_{\tilde{k}m} |m\rangle, \end{aligned} \quad (1)$$

where  $\epsilon_k$  is the eigenvalue of the initially occupied orbital  $|k\rangle$ . The Fock operator is defined as  $\hat{f} \stackrel{\text{def}}{=} \hat{h} + \hat{J}_{mm} - \hat{K}_{mm}$ , with the one-body Hamiltonian containing the interaction with the external laser field,  $\hat{h} \stackrel{\text{def}}{=} p^2/2 + \hat{V}_C(\mathbf{r}) + \hat{V}_L$ ,  $\hat{V}_L \stackrel{\text{def}}{=} \mathbf{F}(t) \cdot \mathbf{r}$ , and  $\hat{J}_{cd}$  and  $\hat{K}_{cd}$  are the *direct* and *exchange interaction* potentials, respectively (see Appendix A 1). The Lagrange multipliers  $\lambda_{\tilde{k}m}$  in Eq. (1) ensure that  $|\tilde{k}\rangle$  at all times remains orthogonal to all initially occupied orbitals  $|m\rangle$ . To implement spin-orbit coupling, instead of resorting to the full four-component Dirac-Fock treatment (RTDCIS [13]), we rely on the phenomenological two-component treatment of Peterson *et al.* [14]. It includes corrections due to scalar-relativistic effects, and at the same time reduces the number of electrons we need to treat explicitly. It replaces the scalar potential  $\hat{V}_C$  by the relativistic effective core potential (RECP), which models the

\*stefanos@mbi-berlin.de; stefanos.carlstrom@matfys.lth.se

Published by the American Physical Society under the terms of the [Creative Commons Attribution 4.0 International](https://creativecommons.org/licenses/by/4.0/) license. Further distribution of this work must maintain attribution to the author(s) and the published article's title, journal citation, and DOI. Funded by [Bibsam](https://www.bibsam.de/).

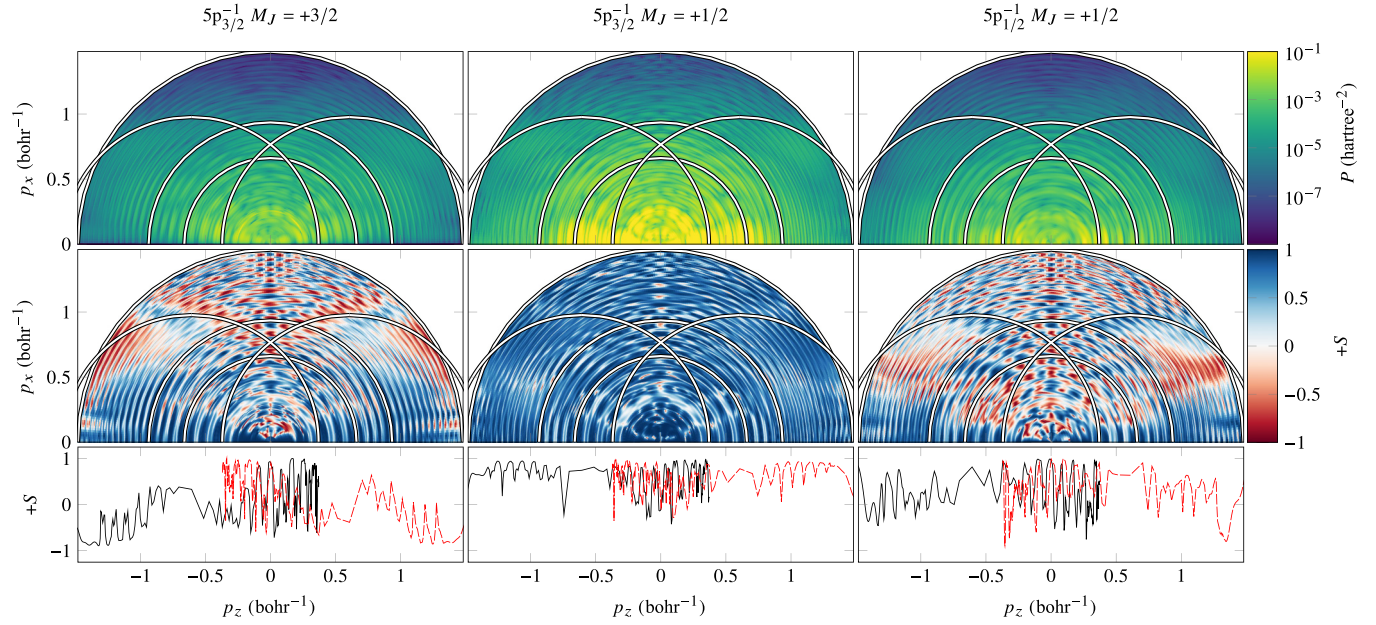


FIG. 1. Top row: Angularly resolved ATI spectra from xenon, correlated to different ionic channels. Middle row: Spin polarization of the photoelectrons; for  $M_J < 0$ , the spin polarization is exactly the opposite of the positive case. Blue color means excess of spin-up (spin-down) for  $+S$  ( $-S$ ), and vice versa for red. The overlaid concentric circles indicate return momenta at the detector corresponding to kinetic energies  $2U_p$ ,  $4U_p$ , and  $10U_p$ , respectively. The offset circles mark the contribution of recolliding electrons with the maximum possible return energy  $W_{k,\max}$ . Bottom row: Lineouts along the  $W_{k,\max}$  circles in the middle row; the black solid (red dashed) line corresponds to initial ionization towards positive (negative)  $p_z$ .

atomic nucleus and the  $1s$ – $3d$  electrons of xenon according to

$$\hat{V}^{\text{RECP}}(\mathbf{r}) = \hat{V}^{\text{scalar}}(r) + \mu \hat{V}_{\ell j}^{s-o}(r). \quad (2)$$

The RECP allows us to identify effects associated with spin-orbit dynamics by scaling the spin-orbit splitting as

$$\Delta E_{s-o}(\mu) \approx \mu \Delta E_{s-o}(1), \quad (3)$$

where  $\Delta E_{s-o}(1) \approx 1.4 \text{ eV}$  is the nominal spin-orbit splitting of the ionic ground state at the CIS level; the dependence is essentially linear in  $\mu$  (see Appendix A 2).

The spin polarization is given by

$$S_I(E, \theta) \stackrel{\text{def}}{=} \frac{P_{I\alpha}(E, \theta) - P_{I\beta}(E, \theta)}{P_{I\alpha}(E, \theta) + P_{I\beta}(E, \theta)},$$

where  $P_{I\sigma}(E, \theta)$  is the ion-, kinetic energy-, angle-, and spin-resolved photoelectron distribution (see Appendix A 3).

### III. CALCULATIONS

We study above-threshold ionization (ATI) from xenon, with the following ionization channels included:  $5p_{3/2}^{-1}$ ,  $M_J = \pm 3/2$ ,  $\pm 1/2$ , and  $5p_{1/2}^{-1}$ ,  $M_J = \pm 1/2$  [15]. Ionization from  $5s$  and lower-lying orbitals is strongly suppressed in the laser fields we consider [ $\hbar\omega = \Delta E_{s-o}(1)$  and  $I_0 = 44 \text{ TW/cm}^2$ ]. The *spin-mixed* channels  $5p_{3/2}^{-1}$ ,  $M_J = \pm 1/2$  (formed from linear combinations of  $p_{0\alpha}$ ,  $p_{+\beta}$  and  $p_{0\beta}$ ,  $p_{-\alpha}$ , respectively) are preferentially ionized, since ionization in linearly polarized fields is dominated by  $p_0$  [16].

The weaker channels  $5p_{3/2}^{-1}$ ,  $M_J = \pm 3/2$  are expected to be *spin pure*, since in order to form the orbitals  $5p_{3/2}$ ,  $m_j = \pm 3/2$ , the orbital- and spin-angular momenta must be maximally aligned ( $p_{+\alpha}$  and  $p_{-\beta}$ , respectively). Linearly

polarized electric fields preserve spin, and thus we expect that the outgoing electron is spin-pure as well. However, the results of our numerical simulations are surprising: only direct, on-axis photoelectrons maintain their expected spin (see Fig. 1). In contrast, electrons that have undergone recollision with the parent ion, and are able to travel off-axis, exhibit substantial amounts of the opposite spin.

To explain this behavior, we posit that this effect results from the recollision of the returning electron off of the ion, which in the spin-mixed channels has time-evolving spin [1,5]. Directly after ionization, the ion has a spin opposite that of the photoelectron, yielding vanishing spin overall. If upon return, the electron finds an ion with a spin different from that at the time of ionization, inelastic scattering into the spin-pure channels of opposite spin in these channels. Furthermore, this apparent spin flip will predominantly occur when  $\Delta E_{s-o}\tau \approx \pi$ , where  $\tau$  is the excursion time of the electron, see Fig. 2 and the SI (see Appendix B). This dynamic corresponds to the spin-orbit clock in the ion undergoing half a revolution.

To investigate this hypothesis in a minimally invasive manner, we tune the spin-orbit splitting  $\Delta E_{s-o}$  by changing the value of  $\mu$  in (2), while keeping all remaining parameters constant. We then find

$$\pi \approx \Delta E_{s-o}(\mu)\tau = \frac{\Delta E_{s-o}(\mu)}{\omega} \omega\tau = \frac{\Delta E_{s-o}(\mu)}{\Delta E_{s-o}(1)} \omega\tau, \quad (4)$$

since we chose the photon energy to be in resonance with the nominal spin-orbit splitting,  $\omega = \Delta E_{s-o}(1)$ . Using (3), we get

$$\mu \approx \frac{\Delta E_{s-o}(\mu)}{\Delta E_{s-o}(1)} \approx \frac{\pi}{\omega\tau}. \quad (5)$$

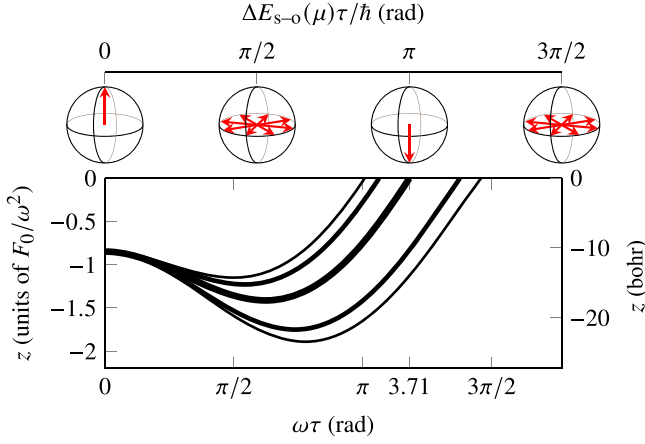


FIG. 2. Sketch of the proposed spin-flipping mechanism; the electron moves along a rescattering trajectory with an excursion phase of  $\omega\tau$ , which in the example is chosen such that the trajectory with maximum return energy  $W_{k,\max}$ , shown as the heaviest line, matches half a revolution of the spin-orbit clock, illustrated as Bloch spheres. The classical trajectories start at the tunnel exit of a Coulombic barrier.

For electrons returning with maximal kinetic energy,  $W_{k,\max}$ , which return at  $\omega\tau \approx 3.71$ , we obtain  $\mu \approx 0.85$ . It is easy to find those final momenta (combinations of  $p_z$  and  $p_x$ ) which result from trajectories recolliding with  $W_{k,\max}$  [17] (see Appendix B); these are marked in Fig. 1 with circles in the forward ( $p_z > 0$ ) and backward ( $p_z < 0$ ) directions. If we take lineouts of the spin polarization along these circles, we predominantly measure the contribution of trajectories returning with  $W_{k,\max}$  kinetic energy. The red streaks in Fig. 1 that indicate the opposite spin do not fall perfectly on the  $W_{k,\max}$  circle; this is mostly due to the circle being derived for classical trajectories with no potential present. The slight shift in momentum for the apparent spin flips is a result of Coulomb focusing.

We thus expect large amounts of opposite spin in the high-rescattering region ( $|W_k| > 4U_p$ ), for  $\mu \approx 0.85$ , since the spin-orbit clock has undergone half a revolution by the time the electron returns. In Fig. 3 we see that this is indeed the case in the spin-pure channels  $5p_{3/2}^{-1}$ ,  $M_J = \pm 3/2$ . Generalizing this argument, for  $\mu \approx \frac{n\pi}{\omega\tau} = 0.85, 1.69, 2.54, 3.40, 4.23, 5.07, \dots$ , we expect to see enhancement and suppression of the opposite spin for odd  $n$  and even  $n$ , respectively.

It is also interesting to note that for  $\mu = 0$ , the photoelectrons in the spin-pure channel are spin-pure as well. In this case, the period of the spin-orbit clock is  $\frac{2\pi}{\Delta E_{s-o}(0^+)} = +\infty$ , and the hole remains forever in its initial spin state, preventing any opposite spin appearing in the spin-pure channels. To further explore the proposed mechanism, we selectively remove the Coulomb repulsion interaction from the EOMs (1); first we exclude exchange-type interactions between ionization channels by dropping the  $\hat{K}_{lk}$  term, and then the direct-type interchannel interactions  $\hat{J}_{lk}$ . Dropping the self-interaction correction  $\hat{K}_{mm}$  does not influence the spin polarization appreciably (see Appendix C 1). The intrachannel interactions  $\hat{J}_{mm}$  must remain, since otherwise the problem would reduce to a

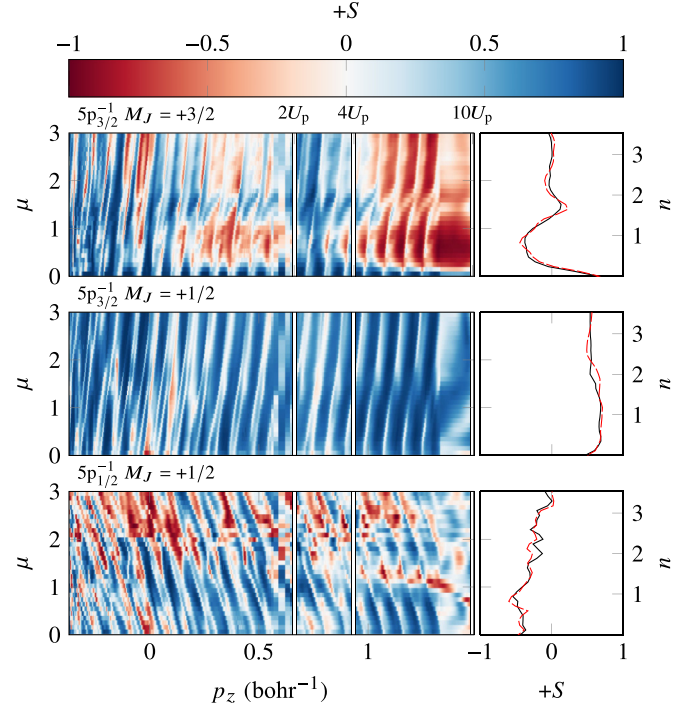


FIG. 3. Lineouts along the  $W_{k,\max}$  circles in Fig. 1, for a range of values of the spin-orbit scaling parameter  $\mu$  [see Eq. (3)], plotted as a function of  $p_z$ ; note that  $2W_k = p_z^2 + p_x^2$ , and the lineouts are *not* taken along constant  $p_x$ . As in Fig. 1, for  $M_J < 0$ , the spin polarization is exactly  $-S$ . Each row corresponds to a specific ion channel; top row: spin-pure channel  $5p_{3/2}^{-1}$ ,  $M_J = +3/2$ ; middle row:  $5p_{3/2}^{-1}$ ,  $M_J = +1/2$ ; bottom row:  $5p_{1/2}^{-1}$ ,  $M_J = +1/2$ . The left column shows emission in the forward direction, i.e., positive final  $p_z$  [due to the long pulse duration,  $\tau = 15$  fs, the spin polarization is almost symmetric about  $p_z = 0$  (see Appendix B 1)]. The right column shows the integrated spin polarization along the lineout, from  $p^2/2 = 4U_p$  to  $p_{\max}$ ; the solid black line corresponds to forward emission, and the dashed red to backward emission. The right ordinate indicate the expected positions corresponding to  $n \approx \mu\omega\tau/\pi$  half-revolutions of the spin-orbit clock, for  $\omega\tau \approx 3.71$  (see main text).

hydrogenic one with a bare xenon nucleus. We compare these instrumented calculations with the full Hamiltonian in Fig. 4. As we see in the figure, the largest effect is the removal of  $\hat{J}_{lk}$ , which is the only term of the three which is long range ( $\hat{K}$ , being traceless, decays at least as quickly as  $r^{-2}$ ). We also note that the removal of  $\hat{K}_{lk}$  quantitatively changes the angular distribution of the spin polarization, even enhancing it, which suggests that  $\hat{K}_{lk}$  actually works *counter* to the proposed mechanism.

We now understand the mechanism leading to the opposite spin in the spin-pure channel better: The hole in this channel is also spin pure, and as such does not undergo any spin oscillation in the spin-orbit clock. However, the holes in the other channels are spin mixed, and the spin-orbit clock oscillates with the period  $T_{s-o} \stackrel{\text{def}}{=} \frac{2\pi}{\Delta E_{s-o}(\mu)}$ . After rescattering at the right moment, we may observe opposite spins due to inelastic scattering into  $5p_{3/2}^{-1}$ ,  $M_J = \pm 3/2$ . Removing  $\hat{J}_{lk}$  from the EOMs (1) suppresses inelastic scattering, and thus precludes any transfer of spin between channels, as we see in



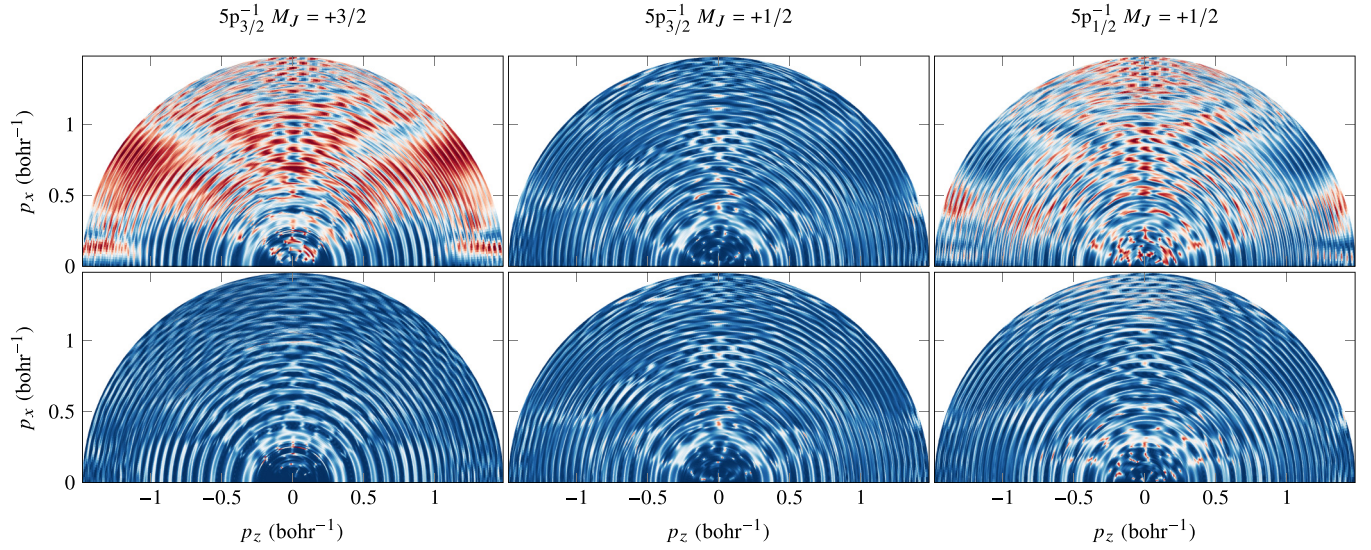


FIG. 4. Effect on the spin polarization when gradually removing the Coulomb electron-electron repulsion interaction from the EOMs (1). Top row:  $\hat{K}_{lk}$  dropped; bottom row;  $\hat{K}_{lk}, \hat{J}_{lk}$  dropped. See the second row of Fig. 1 for the case where all terms in the Hamiltonian are included.

Fig. 4. This mechanism can be semiquantitatively investigated by considering the explicit time-spin dependence of  $\hat{J}_{lk}$  and  $\hat{K}_{lk}$  in  $LS$  coupling, where the orbitals  $l$  and  $k$  change their spin with the period  $T_{s-o}$  (see Appendix C 2).

#### IV. CONCLUSIONS

In conclusion, we have demonstrated that we can generate spin-polarized electrons, even when ionizing using linearly polarized light, as long as we detect the photoelectrons in coincidence with the ion. Furthermore, due to the recollision mechanism in strong-field ionization, we are also able to control the spin of the photoelectron, by tuning the ratio of the spin-orbit splitting and the angular frequency of the

driving field. This mechanism has important implications for recollision-based imaging techniques such as laser-induced electron diffraction, which use the energy- and angle-resolved distribution of the photoelectron to infer the state of the ion; through the spin-orbit interaction, the spin of the photoelectron would reveal additional information on the entangled photoion.

#### ACKNOWLEDGMENTS

S.C. would like to thank Edvin Olofsson for illuminating discussions. The work of S.C. has been supported through scholarship 185-608 from Olle Engkvists Stiftelse. J.M.D. acknowledges support from the Knut and Alice Wallenberg Foundation (Grants No. 2017.0104 and No. 2019.0154), the Swedish Research Council (Grant No. 2018-03845), and Olle Engkvists Stiftelse (Grant No. 194-0734). M.I. acknowledges support from Horizon 2020 research and innovation (Grant No. 899794). O.S. acknowledges support from Horizon Europe ERC-2021-ADG (Grant No. 101054696 Ulisses).

#### APPENDIX A: METHODS

##### 1. Coulomb repulsion

The *direct* and *exchange interaction* potentials are defined by their action on a spin-orbital

$$\hat{J}_{cd}|e\rangle \stackrel{\text{def}}{=} \chi_e(\varsigma_1) \int \frac{d\varsigma_2}{|\mathbf{r}_1 - \mathbf{r}_2|} \chi_c^*(\varsigma_2) \chi_d(\varsigma_2),$$

$$\hat{K}_{cd}|e\rangle \stackrel{\text{def}}{=} \chi_d(\varsigma_1) \int \frac{d\varsigma_2}{|\mathbf{r}_1 - \mathbf{r}_2|} \chi_c^*(\varsigma_2) \chi_e(\varsigma_2) \equiv \hat{J}_{ce}|d\rangle, \quad (\text{A1})$$

where  $\varsigma_{1,2}$  refer to both the spatial and spin coordinates.

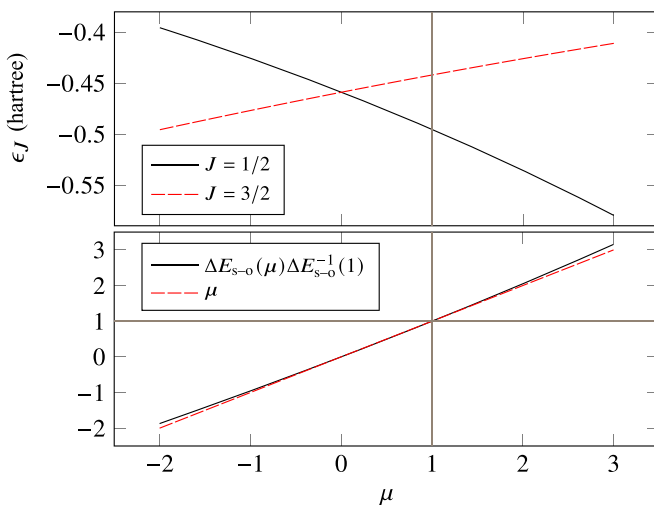


FIG. 5. Spin-orbit splitting  $\Delta E_{s-o}(\mu) \stackrel{\text{def}}{=} \epsilon_{3/2}(\mu) - \epsilon_{1/2}(\mu)$  between  $5p_{3/2}^{-1}$  and  $5p_{1/2}^{-1}$ , as a function of the scaling parameter  $\mu$  in Eq. (2).

TABLE I. Calculated ionization potentials of the  $5s$ ,  $5p$  electrons of xenon, compared with their experimental and relativistic configuration-interaction singles (RCIS) values.

Hole	$I_p$ (eV)	Exp. (eV)	$\Delta$ (eV)	RCIS $I_p$ (eV)
$5p_{3/2}^{-1}$	12.026	12.130 <sup>a</sup>	-0.104	11.968 <sup>c</sup>
$5p_{1/2}^{-1}$	13.483	13.436 <sup>b</sup>	0.047	13.404 <sup>c</sup>
$5s_{1/2}^{-1}$	27.927	23.397 <sup>b</sup>	4.530	27.485 <sup>c</sup>

<sup>a</sup>Reference [20].

<sup>b</sup>Reference [21].

<sup>c</sup>Reference [13].

## 2. Scaling the spin-orbit interaction

The explicit form of the RECP (2) is

$$\begin{aligned}\hat{V}^{\text{RECP}}(\mathbf{r}) &= \hat{V}^{\text{scalar}}(\mathbf{r}) + \mu \hat{V}_{\ell j}^{\text{s-o}}(\mathbf{r}), \\ \hat{V}^{\text{scalar}}(\mathbf{r}) &\stackrel{\text{def}}{=} -\frac{Q}{r} + \hat{V}_{\ell}(r) \hat{P}_{\ell}, \\ \hat{V}_{\ell}(r) &\stackrel{\text{def}}{=} \frac{1}{2\ell + 1} [\ell \hat{V}_{\ell, |\ell - \frac{1}{2}|}(r) + (\ell + 1) \hat{V}_{\ell, \ell + \frac{1}{2}}(r)], \\ \hat{P}_{\ell} &\stackrel{\text{def}}{=} \hat{P}_{\ell, |\ell - \frac{1}{2}|} + \hat{P}_{\ell, \ell + \frac{1}{2}}, \\ \hat{V}_{\ell j}^{\text{s-o}}(\mathbf{r}) &\stackrel{\text{def}}{=} \frac{\Delta \hat{V}_{\ell}(r)}{2\ell + 2} [\ell \hat{P}_{\ell, \ell + 1/2} - (\ell + 1) \hat{P}_{\ell, \ell - 1/2}], \\ \Delta \hat{V}_{\ell}(r) &\stackrel{\text{def}}{=} \hat{V}_{\ell, \ell + 1/2}(r) - \hat{V}_{\ell, \ell - 1/2}(r), \\ \hat{V}_{\ell j} &\stackrel{\text{def}}{=} B_{\ell j}^k \exp(-\beta_{\ell j}^k r^2),\end{aligned}\quad (\text{A2})$$

where  $Q = 26$  is the residual charge,  $\hat{P}_{\ell j}$  is a projector on the spin-angular symmetry  $\ell j$ , and  $B_{\ell j}^k$  and  $\beta_{\ell j}^k$  are numeric coefficients found by fitting to multiconfigurational Dirac-Fock all-electron calculations of the excited spectrum [18,19].

In Fig. 5, we show the effect of scaling the spin-orbit interaction in the RECP (A2). The resultant spin-orbit splitting is essentially proportional to  $\mu$ . In Table I, the calculated ionization potentials for the case  $\mu = 1$  are compared with experimental values from the literature.

## 3. Photoelectron spectra

The photoelectron distributions, resolved on ion state  $I$ , photoelectron energy  $E$ , the angle  $\theta$  with respect to the polarization axis, and with spin projection  $\sigma_z$ , are obtained by tracing over the reduced density matrix:

$$P_{I\sigma_z}(E, \theta) \stackrel{\text{def}}{=} \int d\phi \langle \sigma_z | \hat{\rho}_{II}(E, \theta, \phi) | \sigma_z \rangle. \quad (\text{A3})$$

The density matrix is formed from the outer product of the wave function with itself,

$$\hat{\rho}(E, \theta, \phi) \stackrel{\text{def}}{=} |\Psi(\mathbf{k})\rangle \langle \Psi(\mathbf{k})|, \quad (\text{A4})$$

using the close-coupling ansatz [22] for the wave function

$$|\Psi(\mathbf{k})\rangle = c_{I\ell\sigma_z} \mathcal{A}|I\rangle |\mathbf{k}\sigma_z\rangle, \quad (\text{A5})$$

where  $|I\rangle$  is the state of the ion,

$$\mathbf{k} = \begin{bmatrix} k \sin \theta \cos \phi \\ k \sin \theta \sin \phi \\ k \cos \theta \end{bmatrix}, \quad k = \sqrt{2E}$$

is the asymptotic momentum of the photoelectron,  $\sigma_z$  the spin projection of the photoelectron, and  $\mathcal{A}$  the antisymmetrization operator. The reduced density matrix is obtained from the full density matrix by projecting on specific ion states:

$$\hat{\rho}_{IJ} \stackrel{\text{def}}{=} \langle I | \hat{\rho} | J \rangle. \quad (\text{A6})$$

The decomposition (A5) is computed [12] using the time-dependent surface flux (tSURFF) [23–27] and infinite-time surface flux (iSURFV) [28] techniques, with Volkov asymptotics.

## APPENDIX B: CLASSICAL TRAJECTORIES

Here we rederive the classical trajectories of a free electron in a monochromatic electric field

$$\mathbf{F}(t) = \mathbf{F}_0 \cos(\omega t);$$

these results have been presented many times, most notably by Corkum [29].

We introduce the free oscillation range and the velocity amplitude:

$$\boldsymbol{\alpha} \stackrel{\text{def}}{=} \frac{\mathbf{F}_0}{\omega^2}; \quad \mathbf{v}_0 \stackrel{\text{def}}{=} \frac{\mathbf{F}_0}{\omega};$$

(we note that  $v_0^2 = 4U_p$ ), as well as the phases  $\phi = \omega t$ ,  $\phi_i = \omega t_i$ , and  $\phi_r = \omega t_r$ ,  $\delta\phi = \phi_r - \phi_i \equiv \omega\tau$ , etc.

We find the trajectories by integrating Newton's equations  $\mathbf{a}(t) = -\mathbf{F}(t)$ , neglecting the influence of the atomic potential:

$$\mathbf{v}(t) = -\mathbf{F}_0 \int_{t_i}^t dt' \cos \phi' = -\mathbf{v}_0 (\sin \phi - \sin \phi_i),$$

$$\mathbf{r}(t) = \mathbf{r}_0 + \boldsymbol{\alpha} [\cos \phi - \cos \phi_i + (\phi - \phi_i) \sin \phi_i].$$

The phase of ionization  $\phi_i$  is found for each rescattering phase  $\phi_r$  by requiring that the electron returns to the origin before rescattering:

$$\mathbf{r}(t_r) = 0,$$

which we solve numerically using the gradient method.

The kinetic energy of the electron (before rescattering) is given by

$$W_k(t) = \frac{v^2(t)}{2} \equiv 2U_p (\sin \phi - \sin \phi_i)^2. \quad (\text{B1})$$

We may choose the initial position at the tunnel exit

$$r_0^{\text{tri}} = -\frac{I_p}{F_0},$$

$$\text{or} \quad r_0^{\text{Coul}} = -\frac{I_p}{2F_0} - \sqrt{\left(\frac{I_p}{2F_0}\right)^2 - \frac{2I_p}{F_0}}, \quad (\text{B2})$$

which will give maximal kinetic energies at the time of rescattering, rather different from when the electron starts at the

TABLE II. Influence of the initial position on the maximal kinetic energy upon rescattering, for  $F_0 = 3.5408 \times 10^{-2}$  au and  $\omega = 0.0535$  Ha.

Barrier	$r_0$ (bohr)	$W_{k,\max}(U_p)$	$\phi_i$ (rad)	$\phi_r$ (rad)	$\delta\phi$ (rad)
None	0.0	3.17	0.31	4.40	4.08
Triangular	-12.96	4.69	0.68	4.27	3.59
Coulomb	-10.49	4.36	0.59	4.30	3.71

origin  $r_0 = 0$  (see Table II and Fig. 6), and in turn influence the final momenta on the detector which upon rescattering had the maximal kinetic energy (see Fig. 7). Accounting for the initial position is an important improvement compared to starting at the origin as done by Spanner *et al.* [17], since it allows us to correctly sample the off-axis spin-flip features as seen in Fig. 1 of the main text; for the figures shown there, we use the initial position  $r_0^{\text{Coul}}$  for a Coulombic barrier.

### Lineouts in the backward emission direction

In Fig. 8, the lineouts along the  $W_{k,\max}$  circles in the backward emission direction are shown. Due to the long pulse duration ( $\tau = 15$  fs), the spin polarization in the backward direction is almost a perfect mirror image of the forward distribution, as evidenced by the similarity of the integrated lineouts also shown in the figure.

## APPENDIX C: SCATTERING MATRIX ELEMENTS

### 1. Effect of removing $\hat{K}_{mm}$

See Fig. 9 for the effect of removing  $\hat{K}_{mm}$  from the EOMs; the results do not change appreciably.

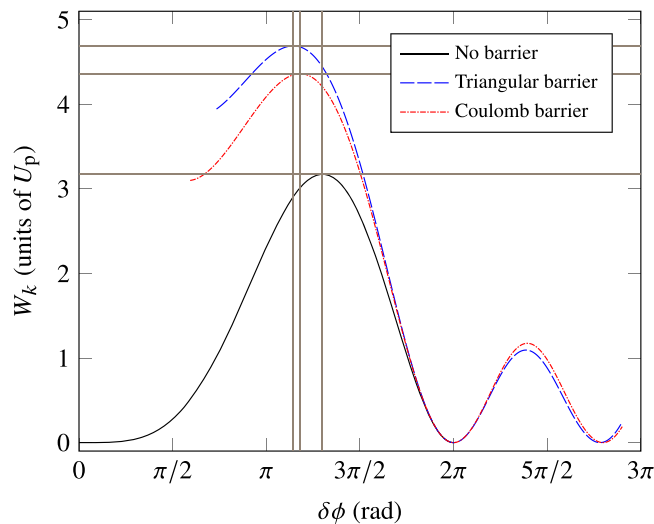


FIG. 6. Kinetic energy upon rescattering as a function of excursion phase, for three different choices of initial starting position (given in Table II).

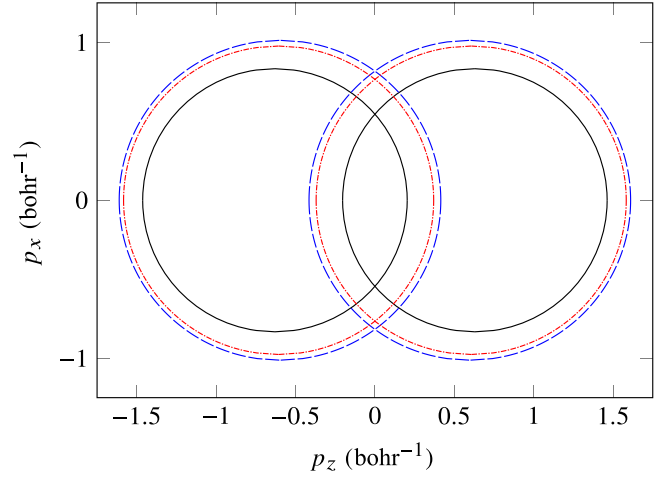


FIG. 7. Final electron momenta corresponding to maximal kinetic energy upon rescattering, for three different choices of initial starting position (line patterns are the same as in Fig. 6).

### 2. Time-dependent scattering matrix elements

Our numerical treatment is done in the  $jj$  coupling basis. We wish to derive an expression for the time-dependent spin flip. The natural basis for this process, the spin-orbit clock, is  $LS$  coupling, where the spin of the hole is “breathing” in time, due to the nondiagonal ionic Hamiltonian. For the  $np^6$  multiplet, the transform between  $LS$  and  $jj$  coupling is given

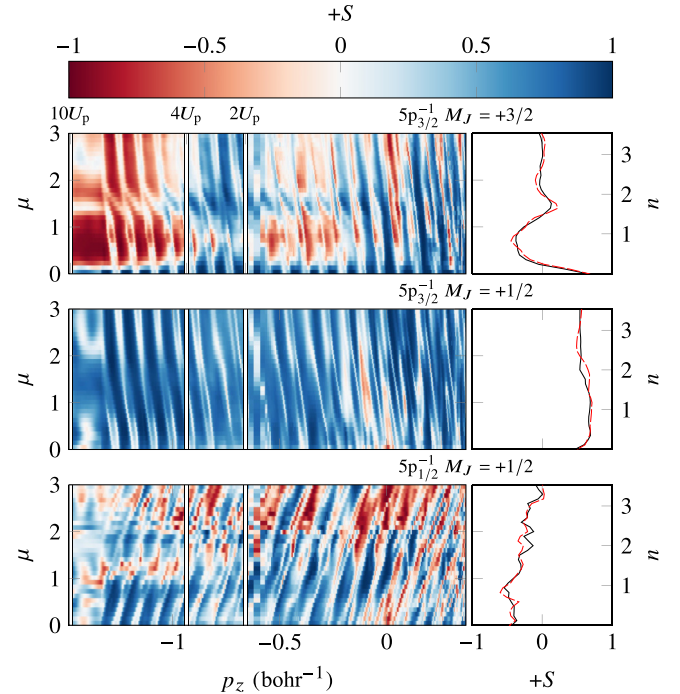


FIG. 8. Similar to Fig. 3 of the main manuscript, but the lineouts are instead along the  $W_{k,\max}$  circles in the backward direction, i.e., negative final  $p_z$ .



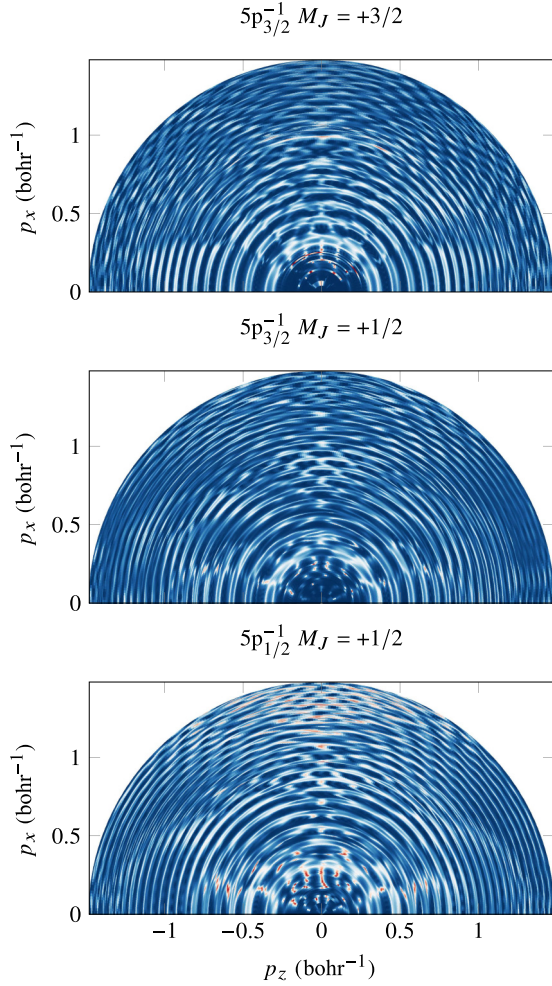


FIG. 9. The effect of removing  $\hat{K}_{mm}$  from the EOMs does not appreciably affect the spin-flipping mechanism; cf. Fig. 4 of the main manuscript.

by (see Table 8.1 of Ref. [30])

$j$	$m_j$	$p_{+\alpha}$	$p_{+\beta}$	$p_{0\alpha}$	$p_{0\beta}$	$p_{-\alpha}$	$p_{-\beta}$
$\frac{3}{2}$	$\frac{3}{2}$	1					
$\frac{3}{2}$	$\frac{1}{2}$		$\sqrt{\frac{1}{3}}$	$\sqrt{\frac{2}{3}}$			
$\frac{1}{2}$	$\frac{1}{2}$		$\sqrt{\frac{2}{3}}$	$-\sqrt{\frac{1}{3}}$			
$\frac{3}{2}$	$-\frac{1}{2}$			$\sqrt{\frac{2}{3}}$	$\sqrt{\frac{1}{3}}$		
$\frac{1}{2}$	$-\frac{1}{2}$			$\sqrt{\frac{1}{3}}$	$-\sqrt{\frac{2}{3}}$		
$\frac{3}{2}$	$-\frac{3}{2}$						1

(C1)

which clearly shows that the  $J = \frac{3}{2}$ ,  $M_J = \pm\frac{3}{2}$  channels are spin pure. Similarly, the ionic spin-orbit Hamiltonian within

this multiplet is in  $jj$  coupling

$$\hat{H}_{s-o}^{(jj)} = \begin{bmatrix} 0 & & & & \\ & 0 & & & \\ & & -\Delta E_{s-o} & & \\ & & & 0 & \\ & & & & -\Delta E_{s-o} \\ & & & & & 0 \end{bmatrix}, \quad (C2)$$

the propagator of which in  $LS$  coupling is given exactly by

$$\exp[-i\hat{H}_{s-o}^{(LS)}(t-t_i)] = \begin{bmatrix} 1 & & & & & \\ & a & b & & & \\ & b & c & & & \\ & & & c & b & \\ & & & b & a & \\ & & & & & 1 \end{bmatrix}, \quad (C3)$$

where

$$a \stackrel{\text{def}}{=} \frac{1}{3}(1+2e^{i\phi}), \quad b \stackrel{\text{def}}{=} \frac{\sqrt{2}}{3}(1-e^{i\phi}), \quad c \stackrel{\text{def}}{=} \frac{1}{3}(2+e^{i\phi}), \quad (C4)$$

and  $\phi = \Delta E_{s-o}(t-t_i)$ .

The matrix element responsible for the inelastic scattering between channels is given by

$$[l\tilde{k}|k\tilde{l}] \equiv [l\tilde{k}|k\tilde{l}] - [l\tilde{k}|\tilde{l}k], \quad (C5)$$

the first term of which corresponds to the *direct interaction* and the second term to the *exchange interaction*. As shown in the above, when dropping  $\hat{J}_{lk}$  from the EOMs, the spin-flipping mechanism was almost completely suppressed, which is why we will focus on  $[l\tilde{k}|k\tilde{l}]$ , from which  $\hat{J}_{lk}$  originates [12].

Assume we initially ionize the  $|l(t_i)\rangle = |p_{+\beta}\rangle$  orbital (a component of the  $j = 3/2$ ,  $m_j = 1/2$  orbital); then, neglecting any effect of the spin-orbit interaction on the free electron,  $|\tilde{l}\rangle$  will be a  $\beta$  electron, while the associated hole will evolve in time according to

$$|l(t)\rangle = a|p_{+\beta}\rangle + b|p_{0\alpha}\rangle. \quad (C6)$$

Simultaneously, the channel we consider scattering *into*, the spin-pure  $j = 3/2$ ,  $m_j = 3/2$ , has a time-independent hole, also in  $LS$  coupling:

$$|k(t)\rangle = |p_{+\alpha}\rangle. \quad (C7)$$

From this, we deduce that the direct part of the scattering matrix element (C5), responsible for the apparent spin flip, is

$$\begin{aligned} |[l\tilde{k}|k\tilde{l}]|^2 &= \left| a \underbrace{[p_{+\beta}; \tilde{k}\sigma_z|p_{+\alpha}; \tilde{l}\beta]}_0 + b[p_{0\alpha}; \tilde{k}\sigma_z|p_{+\alpha}; \tilde{l}\beta] \right|^2 \\ &= \left| \frac{\sqrt{2}}{3}(1-e^{i\phi}) \right|^2 |[p_{0\alpha}; \tilde{k}\sigma_z|p_{+\alpha}; \tilde{l}\beta]|^2 \delta_{\sigma_z\beta} \\ &= \frac{4}{9} [1 - \cos \Delta E_{s-o}(t-t_i)] |[p_{0\alpha}; \tilde{k}\sigma_z|p_{+\alpha}; \tilde{l}\beta]|^2 \delta_{\sigma_z\beta}, \end{aligned} \quad (C8)$$

which will have its maximum when  $\Delta E_{s-o}(t-t_i) = (2q+1)\pi$ , i.e., odd multiples of  $\pi$ .

We would reach a similar conclusion if we instead assumed ionization to start from  $|l(t_i)\rangle = |p_0\beta\rangle$ . This argument can trivially be extended to the exchange interaction  $[\tilde{l}\tilde{k}|\tilde{l}\tilde{k}]$ , and hence also  $||[\tilde{l}\tilde{k}||\tilde{k}\tilde{l}]|^2$ . As a side note, since the orbitals in the

first coordinate of  $[\tilde{l}\tilde{k}|\tilde{k}\tilde{l}]$  in (C8) are both  $p$  electrons, only even orders in the multipole expansion of  $\hat{J}_{\tilde{l}\tilde{k}}$  will contribute. Furthermore, since the orbitals have different components ( $p_0$  versus  $p_+$ ), the lowest order is the quadrupole.

- 
- [1] I. Barth and O. Smirnova, *J. Phys. B: At., Mol. Opt. Phys.* **47**, 204020 (2014).
- [2] A. Hartung, F. Morales, M. Kunitski, K. Henrichs, A. Laucke, M. Richter, T. Jahnke, A. Kalinin, M. Schöffler, L. P. H. Schmidt, M. Ivanov, O. Smirnova, and R. Dörner, *Nat. Photonics* **10**, 526 (2016).
- [3] D. Trabert, A. Hartung, S. Eckart, F. Trinter, A. Kalinin, M. Schöffler, L. P. H. Schmidt, T. Jahnke, M. Kunitski, and R. Dörner, *Phys. Rev. Lett.* **120**, 043202 (2018).
- [4] Z. Nie, F. Li, F. Morales, S. Patchkovskii, O. Smirnova, W. An, N. Nambu, D. Matteo, K. A. Marsh, F. Tsung, W. B. Mori, and C. Joshi, *Phys. Rev. Lett.* **126**, 054801 (2021).
- [5] N. Mayer, S. Beaulieu, Á. Jiménez-Galán, S. Patchkovskii, O. Kornilov, D. Descamps, S. Petit, O. Smirnova, Y. Mairesse, and M. Y. Ivanov, *Phys. Rev. Lett.* **129**, 173202 (2022).
- [6] T. Zuo, A. Bandrauk, and P. Corkum, *Chem. Phys. Lett.* **259**, 313 (1996).
- [7] Y. Huismans, A. Rouzee, A. Gijsbertsen, J. H. Jungmann, A. S. Smolkowska, P. S. W. M. Logman, F. Lepine, C. Cauchy, S. Zamith, T. Marchenko, J. M. Bakker, G. Berden, B. Redlich, A. F. G. van der Meer, H. G. Muller, W. Vermin, K. J. Schafer, M. Spanner, M. Y. Ivanov, O. Smirnova *et al.*, *Science* **331**, 61 (2010).
- [8] S. Patchkovskii, Z. Zhao, T. Brabec, and D. M. Villeneuve, *Phys. Rev. Lett.* **97**, 123003 (2006).
- [9] S. Patchkovskii, Z. Zhao, T. Brabec, and D. M. Villeneuve, *J. Chem. Phys.* **126**, 114306 (2007).
- [10] N. Rohringer, A. Gordon, and R. Santra, *Phys. Rev. A* **74**, 043420 (2006).
- [11] L. Greenman, P. J. Ho, S. Pabst, E. Kamarchik, D. A. Mazziotti, and R. Santra, *Phys. Rev. A* **82**, 023406 (2010).
- [12] S. Carlström, M. Spanner, and S. Patchkovskii, *Phys. Rev. A* **106**, 043104 (2022); S. Carlström, M. Bertolino, J. M. Dahlström, and S. Patchkovskii, *ibid.* **106**, 042806 (2022).
- [13] F. Zapata, J. Vinbladh, A. Ljungdahl, E. Lindroth, and J. M. Dahlström, *Phys. Rev. A* **105**, 012802 (2022).
- [14] K. A. Peterson, D. Figgen, E. Goll, H. Stoll, and M. Dolg, *J. Chem. Phys.* **119**, 11113 (2003).
- [15] The quantum numbers  $J$  and  $M_J$  pertain to the states of the ion, whereas  $j$  and  $m_j$  label the initially occupied orbitals; for CIS from closed valence shells,  $J = j$  and  $M_J = -m_j$ . In  $LS$  coupling, the  $p$  spin-orbitals are labeled  $p_{m_\ell}\sigma_z$ , where the possible values for  $m_\ell$  are 0,  $\pm$ , and  $\sigma_z = \alpha, \beta$  corresponding to spin-up and spin-down, respectively.
- [16] A. M. Perelomov, V. S. Popov, and M. V. Terent'ev, *Zh. Eksp. Teor. Fiz.* **50**, 1393 (1966) [*Sov. Phys. JETP* **23**, 924 (1966)].
- [17] M. Spanner, O. Smirnova, P. B. Corkum, and M. Y. Ivanov, *J. Phys. B: At., Mol. Opt. Phys.* **37**, L243 (2004).
- [18] M. Dolg and X. Cao, *Chem. Rev.* **112**, 403 (2011).
- [19] M. Dolg, Relativistic effective core potentials, in *Handbook of Relativistic Quantum Chemistry* (Springer, Berlin, Heidelberg, 2016), pp. 449–478.
- [20] E. B. Saloman, *J. Phys. Chem. Ref. Data* **33**, 765 (2004).
- [21] J. E. Hansen and W. Persson, *Phys. Scr.* **36**, 602 (1987).
- [22] W. Fritsch and C.-D. Lin, *Phys. Rep.* **202**, 1 (1991).
- [23] A. M. Ermolaev, I. V. Puzynin, A. V. Selin, and S. I. Vinitzky, *Phys. Rev. A* **60**, 4831 (1999).
- [24] A. M. Ermolaev and A. V. Selin, *Phys. Rev. A* **62**, 015401 (2000).
- [25] V. V. Serov, V. L. Derbov, B. B. Joulakian, and S. I. Vinitzky, *Phys. Rev. A* **63**, 062711 (2001).
- [26] L. Tao and A. Scrinzi, *New J. Phys.* **14**, 013021 (2012).
- [27] A. Scrinzi, *New J. Phys.* **14**, 085008 (2012).
- [28] F. Morales, T. Bredtmann, and S. Patchkovskii, *J. Phys. B: At., Mol. Opt. Phys.* **49**, 245001 (2016).
- [29] P. B. Corkum, *Phys. Rev. Lett.* **71**, 1994 (1993).
- [30] D. A. Varshalovich, *Quantum Theory of Angular Momentum: Irreducible Tensors, Spherical Harmonics, Vector Coupling Coefficients, 3nj Symbols* (World Scientific, Singapore, 1988).